


Article

Pd-Modified LaFeO₃ as a High-Efficiency Gas-Sensing Material for H₂S Gas Detection

Heng Zhang¹, Jing Xiao^{1,*}, Jun Chen¹, Yan Wang¹, Lian Zhang¹, Shuai Yue¹, Suyan Li¹, Tao Huang¹ and Da Sun^{2,3,*} 

¹ College of Physics and Electronic Engineering, Taishan University, Taian 271000, China; h_zhangabc@163.com (H.Z.); nankaichen@163.com (J.C.); joko365@163.com (Y.W.); alian_1987512@126.com (L.Z.); shuaiyue426@foxmail.com (S.Y.); lisuyansu@163.com (S.L.); thuangdd@sina.com (T.H.)

² Institute of Life Sciences & Biomedical Collaborative Innovation Center of Zhejiang Province, Wenzhou University, Wenzhou 325035, China

³ Zhejiang Provincial Key Laboratory for Water Environment and Marine Biological Resources Protection, National & Local Joint Engineering Research Center for Ecological Treatment Technology of Urban Water Pollution, Wenzhou University, Wenzhou 325035, China

* Correspondence: xiaojingzx@163.com (J.X.); sunday@wzu.edu.cn (D.S.)

Abstract: As a typical *p*-type semiconductor gas-sensing material, LaFeO₃ has good response stability to H₂S, but its responsiveness is low, and the detection limit is not low enough for large-scale use in the field of gas sensors. To obtain better performance, we synthesized Pd modified LaFeO₃ using the sol-gel method. A total of 3 wt% of Pd-LaFeO₃ with a high specific surface area had the highest response to H₂S (36.29–1 ppm) at 120 °C, with relatively fast response–recovery times (19.62/15.22 s), and it had higher selectivity to H₂S with other gases. Finally, we detected the H₂S concentrations in the air around the shrimps, and the H₂S concentrations that we obtained by the 3 wt% Pd-LaFeO₃ in this study were within 10% of those obtained by GC-MS. According to the experimental results, noble-metal surface modification improves the performance of gas-sensing materials, and Pd-LaFeO₃ has considerable potential in H₂S detection.

Keywords: Pd; LaFeO₃; H₂S; sensor; GC-MS



Citation: Zhang, H.; Xiao, J.; Chen, J.; Wang, Y.; Zhang, L.; Yue, S.; Li, S.; Huang, T.; Sun, D. Pd-Modified LaFeO₃ as a High-Efficiency Gas-Sensing Material for H₂S Gas Detection. *Nanomaterials* **2022**, *12*, 2460. <https://doi.org/10.3390/nano12142460>

Academic Editor: Sergei Kulich

Received: 6 June 2022

Accepted: 15 July 2022

Published: 18 July 2022

Publisher's Note: MDPI stays neutral with regard to jurisdictional claims in published maps and institutional affiliations.



Copyright: © 2022 by the authors. Licensee MDPI, Basel, Switzerland. This article is an open access article distributed under the terms and conditions of the Creative Commons Attribution (CC BY) license (<https://creativecommons.org/licenses/by/4.0/>).

1. Introduction

H₂S is a colorless, highly toxic and acidic gas with a particular rotten egg smell, and even low concentrations of H₂S can impair the human sense of smell. In high concentrations, it has no smell (because high concentrations paralyze the olfactory nerve). In addition, H₂S is flammable and typically dangerous [1–8]. H₂S gas is released during the breakdown of food, and it is also responsible for bad breath caused by periodontitis [8–11]. There are about 0.195 ppm H₂S in the exhaled breath of a person with periodontitis and 0.105 ppm in that of a healthy person [12]. Using the nose as a means of detecting H₂S can be fatal. Therefore, the timely detection of very low concentrations of H₂S gas is important.

In recent years, the use of MOSs (metal oxide semiconductor) gas sensors to detect the concentrations of target gases has become increasingly popular. These are similar to smoke sensors in hotels, natural gas alarms in homes, etc. Some MOSs have excellent responses to gases, such as LaFeO₃ [13–16], SmFeO₃ [17–21], PrFeO₃ [22,23], HoFeO₃ [24], NdFeO₃ [25], YCoO₃ [26], BaSnO₃ [27], ZnSnO₃ [28] and YMnO₃ [29]. For H₂S, the gas-sensing materials are as follows: Pt-ZnO [30], Pd-ZnO [31], CuO/SnO₂ [32], Pt-WO₃ [33], WO₃ [34–36], Pt-Fe₂O₃ [37], CuO/CuFe₂O₄ [38], Ag-SnO₂ [39], YMnO₃ [29], Sn-NiO [40], Au-SnO₂ [41], Co₃O₄ [42], Pt-SnO₂ [43], Ag-TiO₂ [44], WO₃ [45], Au-ZnO [46], ZnO/ZnSe [47], Pt-ZnO [48], CoFe₂O₄ [49], Pt-Zn₂SnO₄ [50], etc. MOSs, especially Pd-LaFeO₃ perovskite materials, have the unique advantages of large specific surface areas and abundant active sites, which can promote the diffusion path and increase the adsorption of target gas

molecules, thereby enhancing their sensing abilities. In particular, Pd–LaFeO₃ is widely used in gas sensing, displaying excellent performance, a low detection limit, strong humidity adaptability and long-term stability. According to previously published studies, the response of Pd–LaFeO₃ is as follows: 1.9–1 ppm acetone [51]; 1.2–100 ppm CO [52]. Although there are many reports on the detection of H₂S by gas sensors, the performances of gas-sensing materials to H₂S are generally not sufficient, and the detection limits cannot reach the PPB level, which is a challenge for realistic requirements.

The aim of this study was to obtain a gas-sensing material with a low detection limit and high response rate, selectivity and long-term stability. We synthesized Pd–LaFeO₃ via the sol–gel method and sintered it at 800 °C. Pd–LaFeO₃ had a high specific surface area and porosity, which are two important factors for gas-sensing materials to improve their responses to target gases. Compared with LaFeO₃, Pd–LaFeO₃ showed a higher response to the H₂S gas and compared with other gases, 3 wt% Pd–LaFeO₃ showed high selectivity for H₂S. In addition, Pd nanoparticles as a catalyst greatly enhanced the surface activity of the gas-sensing materials and greatly shortened the response–recovery times. The innovation of this research is in the use of MOS gas sensors to explore the practical applications of H₂S gas detection, which are rarely shown in other reports of MOS gas sensors. We detected the H₂S concentrations in the air around shrimps using a gas sensor, and we compared them with the results obtained by the GC–MS method; the error was within 10%. According to the experimental results, Pd nanoparticles greatly improve the response of LaFeO₃ to H₂S gas, and the detection of H₂S gas by a gas sensor is a feasible and effective method.

2. Materials and Methods

2.1. Preparation and Characterization of Nanocrystalline Pd–LaFeO₃

In Figure 1a, we present the chemical raw materials used in this work. First, we placed the weighed chemical materials (La₂O₃ (32.58 g), Fe(NO₃)₃ (48.4 g), PdCl₂ (7.287 g), PEG (M_w 20,000, 60 g), HNO₃ (97%, 500 mL) and deionized water (1000 mL)) in the beaker, and then we added the solution of HNO₃ for the mixed dissolution over a period of 4 h (Figure 1b). The mixed solution sat for 2 h, and then we placed it in a water bath and stirred it at 80 °C for 24 h to obtain the mixed sol. Then, the mixed sol was removed and pre-sintered at 100 °C for 2 h in a muffle furnace. It was then gridded and sintered again at 800 °C for 6 h in the muffle furnace (Figure 1c). Finally, we obtained the Pd–LaFeO₃ powder (approximately 38 g).

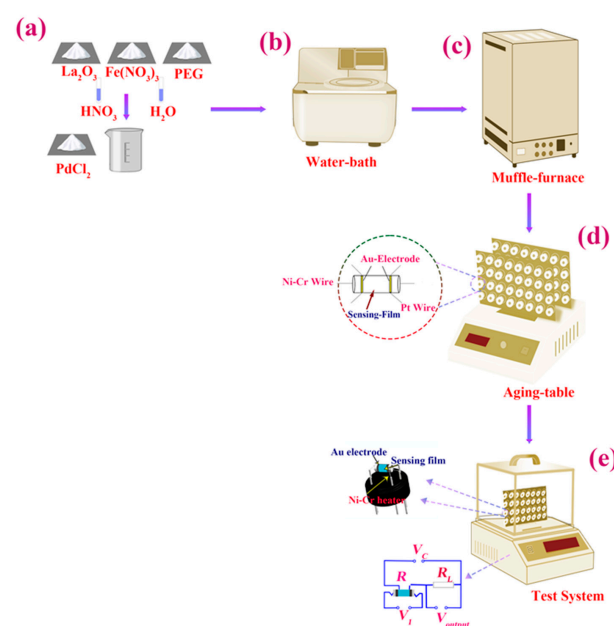


Figure 1. (a–d) Flowchart of Pd–LaFeO₃ preparation; (e) gas-sensor-structure diagram and gas-sensor test system.

2.2. Fabrication and Measurement of Sensor

We mixed the Pd–LaFeO₃ powder with deionized water to produce a paste, and then we placed the paste on a ceramic tube (Al₂O₃), approximately 2 mm in external diameter, 8 mm in length and 1.6 mm in internal diameter, with two electrodes installed at each end (Figure 1d). Then, we placed the whole prepared sensor on the aging table and aged it at 200 °C for 24 h (Figure 1d). After that, we tested the prepared sensor for the targeted gas in the gas-sensor test system (Figure 1e).

2.3. Ready-Made Sensor

In Figure 1e, we present the gas sensor structure diagram and the test circuit of the gas-sensor test system. The Ni–Cr wire was used to heat the sensing material to a higher operating temperature. Au electrodes and Pt wires were used to monitor the resistance of gas-sensing materials in real-time. V_C is the supply voltage, which was kept constant at 5 V; V_1 is the voltage at both ends of the gas sensor; R_I is the value of the variable resistor; V_{output} is the voltage across R_I ; R is the resistance value of the sensor. We calculated R using the following formula:

$$R = \frac{v_1}{v_{output}/R_I}. \quad (1)$$

The gas-sensing response (S) was defined as R_g/R_a : R_g is the resistance of the sensor in the tested gas, and R_a is the resistance of the sensor when it is in the air. We defined the response time as the time taken to attain 90% of the maximum value in the ascending phase and the recovery time as the time taken to regain 10% of the base value in the descending phase. The experimental environment was as follows: RH, 20%; environment temperature, 20 °C.

3. Results

3.1. Material Characterization

In Figure 2a, we present the X-ray diffraction analysis (XRD) (Bruker D8 ADVANCE with a CuK α amount of 1.5405 Å at 40 kV and 40 mA, Berlin, Germany) of the 3 wt% Pd–LaFeO₃. Compared with the standard card (PDF card: 37–1493), the Pd–LaFeO₃ shows a single phase. We can calculate the average particle size by the Scherrer method. The Scherrer equation is as follows:

$$D = \frac{k\lambda}{\beta \cos \theta} \quad (2)$$

where λ is the wavelength of the X-ray, β is the integral width of the diffraction peaks and θ is the Bragg diffraction angle. The average particle size of Pd–LaFeO₃ is about 68.7 nm. Because of the low amount of Pd, the characteristic peak was not reflected in the XRD pattern, so we performed EDS (energy dispersive spectroscopy) for 3 wt% Pd–LaFeO₃ to confirm the presence of Pd. As can be seen in Figure 2b, Pd was present in the material. The atomic compositions of the elements in all samples are shown in Table 1. No other impure elements were present in any of the samples. Figure 2c–f shows the scanning electron microscopy (SEM) (HITACHI SU8010 8.0 kV, Tokyo, Japan) spectra of LaFeO₃ and 3 wt% Pd–LaFeO₃ under different magnifications. The unmodified LaFeO₃ has a common perovskite structure, and the 3 wt% Pd–LaFeO₃ has a network structure.

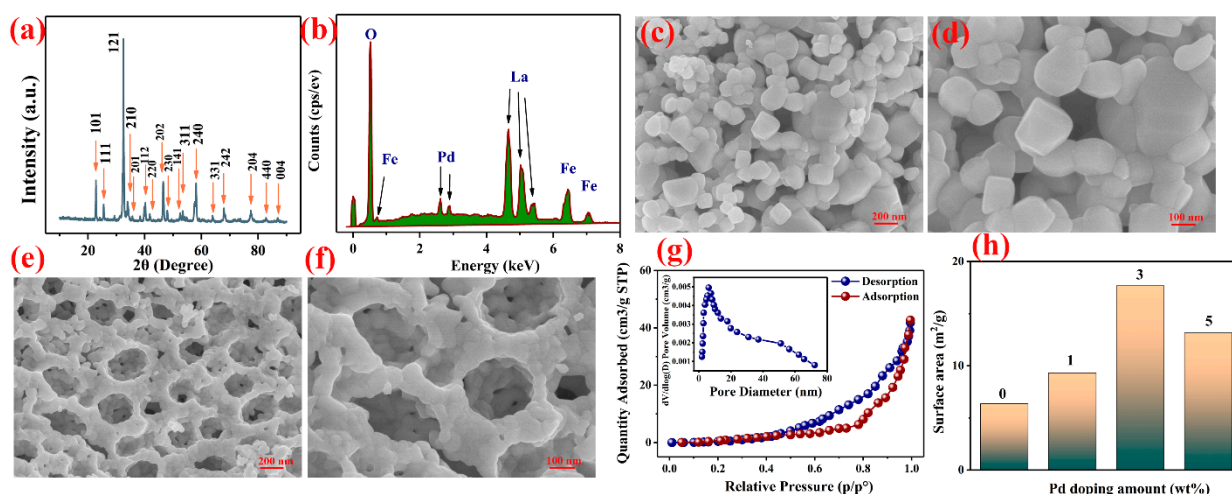


Figure 2. (a) XRD pattern of 3 wt% Pd–LaFeO₃; (b) EDS pattern of 3 wt% Pd–LaFeO₃; (c,d) SEM spectra of pure LaFeO₃; (e,f) SEM spectra of 3 wt% Pd–LaFeO₃; (g) N₂ adsorption–desorption isotherms and pore size distributions (the inset) for 3 wt% Pd–LaFeO₃ nanocomposite; (h) specific surface areas of LaFeO₃ with different amounts of Pd.

Table 1. The atomic compositions (%) of the elements in all samples.

	Pd	La	Fe	O
0	0	19.73	23.68	56.59
1	0.45	19.85	19.99	59.71
3	1.40	19.78	19.70	59.12
5	2.35	19.46	19.56	58.63

To understand which microstructure was more favorable to the properties of the gas-sensing material, we needed to ascertain which structure had a higher specific surface area and porosity. We further analyzed the specific surface area and porosity of the 3 wt% Pd–LaFeO₃ hollow nanofibers by nitrogen adsorption–desorption measurement. In Figure 2g, we present the BET curves for 3 wt% Pd–LaFeO₃ and the corresponding Barrett–Joyner–Halenda (BJH) pore size distribution (inset). The specific surface area of 3 wt% Pd–LaFeO₃ is 17.53 m²/g, and the average pore size is 13.6 nm. We present the specific surface areas of LaFeO₃ with different amounts of Pd in Figure 2h. When the amount of Pd was 3 wt%, the composite powder obtained the largest specific surface area. Because Pd nanoparticles can inhibit the growth of the MOS grain, the smaller the grain size, the larger the specific surface area. However, when the amount of Pd is too high, the particles appear in a small range of agglomerations, and the specific surface area of the material decreases. The specific surface area is an important factor for sensing the properties of materials. A large specific surface area can provide more adsorption sites, which enhances the reactions between the sensing material and gas molecules, which results in a high response to the test gas.

The X-ray photoelectron spectroscopy (XPS) spectra for the presence of Pd in the material are shown in Figure 3. The spectra consist of two peaks, Pd 3d_{5/2} (335.8 eV) and Pd 3d_{3/2} (341.3 eV). The Pd 3d_{5/2} peak consists of a high-intensity peak at 335.6 eV, related to Pd⁰, and a low-intensity peak at 336.5 eV, related to Pd²⁺. The Pd 3d_{3/2} also consists of two peaks, at 341.1 and 341.9 eV. Additionally, this can also indicate Pd is not doped into the lattice of LaFeO₃; therefore, Pd–LaFeO₃ is a composite material.

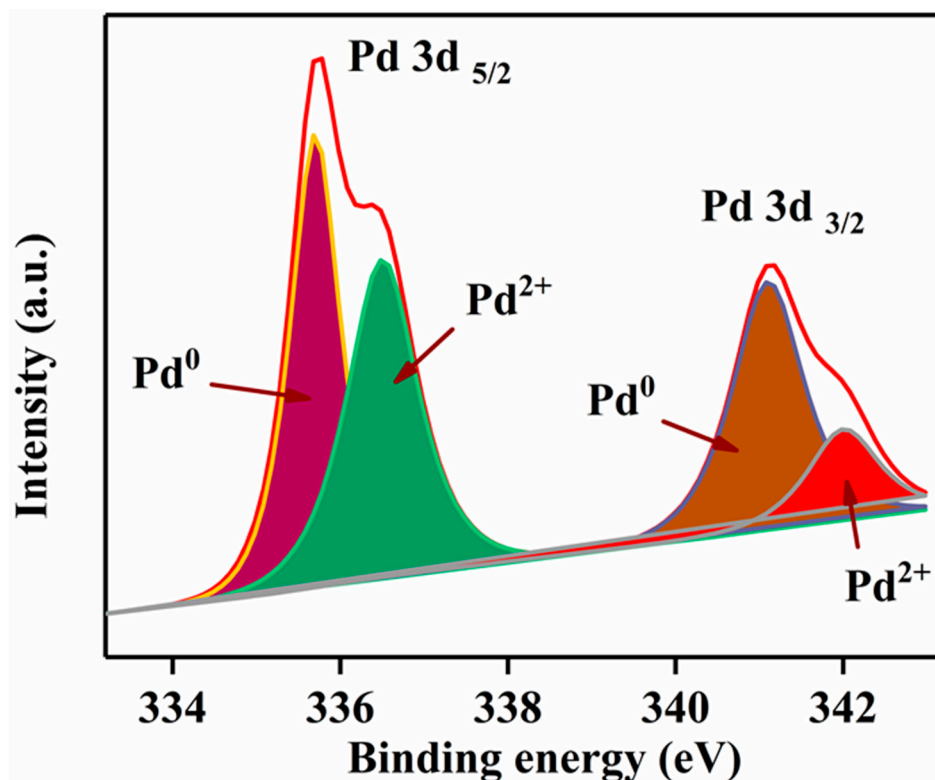


Figure 3. X-ray photoelectron spectroscopy (XPS) of Pd in the material.

3.2. Gas-Sensing Performance

In Figure 4a, we present the response curves of the LaFeO₃ with different amounts of Pd to 1 ppm H₂S with the operating temperatures. For all the samples, we obtained the highest responses at 120 °C. The highest responses to 1 ppm H₂S were 8.26 (0 wt% Pd), 17.85 (1 wt% Pd), 36.29 (3 wt% Pd) and 23.26 (5 wt% Pd). The responses were more than four times higher than before modification with Pd. In Figure 4b–e, we present the responses of all the samples to 0.1–1 ppm H₂S with the operating temperatures. For any H₂S concentration, the optimum operating temperature was 120 °C. In Table 2, we present the responses of the LaFeO₃ with different amounts of Pd.

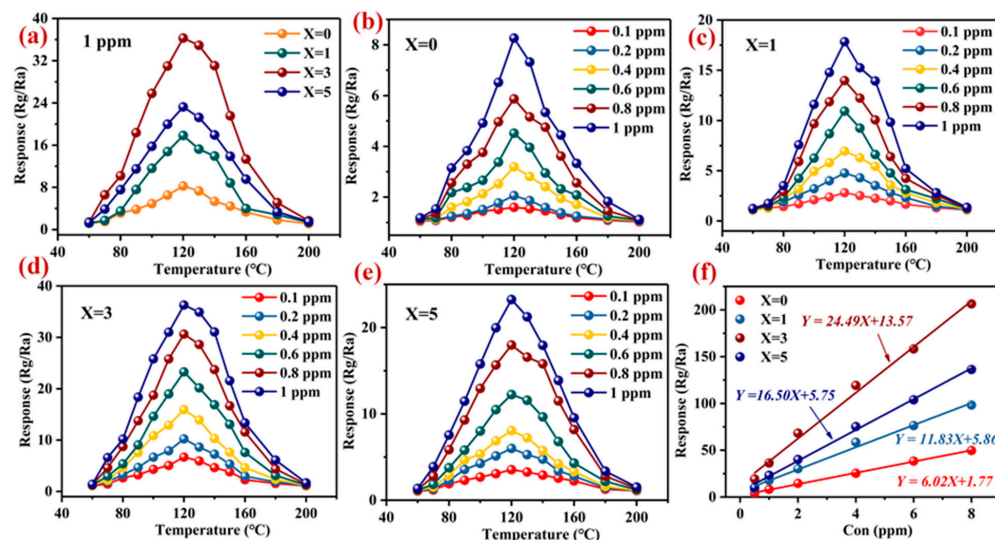


Figure 4. (a) Responses of Pd–LaFeO₃ to 1 ppm H₂S with operating temperatures; (b–e) responses of Pd–LaFeO₃ to different concentrations of H₂S with operating temperature; (f) linear relationship between the responses and H₂S concentrations; X refers to the amount of Pd.

Table 2. Response of LaFeO₃ with different amounts of Pd to H₂S gas.

Pd (wt%)	Con (ppm)						
	0.1	0.2	0.4	0.6	0.8	1	
0	1.59	2.06	3.19	4.52	5.87	8.26	
1	2.8	4.76	6.94	10.93	13.97	17.85	
3	6.69	10.22	15.93	23.27	30.62	36.29	
5	3.53	5.98	8.06	12.25	17.98	23.25	

The relationship between the material's sensitivity and the gas concentration is important, and we can use a high fitting relationship to predict the response value at a given gas concentration. In Figure 4f, we can see the relationship between the responses of Pd-LaFeO₃ to multiple H₂S concentrations. For both the unmodified and modified Pd-LaFeO₃, the responses have a good linear relationship with the gas concentrations and all the R² values are greater than 98%.

Repeatability is another important property that determines whether a gas sensing material is sufficient or not. In Figure 5a–d, we present the repeatability of the responses to different concentrations (0.1–1 ppm) of H₂S gas for Pd-LaFeO₃. All the repeated processes went as follows: When the resistance value of the gas-sensing material was stabilized, we injected the H₂S gas into the reaction chamber, and the resistance of the material increased immediately. After a period of time, the resistance stabilized, we removed the H₂S gas, the resistance of the material decreased immediately and we could restore it to the initial state. For the H₂S gas with different concentrations, we could restore the resistance of the gas-sensing material to the initial value after every time the H₂S gas was removed, which indicated that the material had excellent repeatability. The response–recovery times of all the samples were different at different operating temperatures, which indicated that the operating temperature affected the chemical reaction on the material's surface. We present the response–recovery times of all the samples in Table 3 and Figure 6a–d. The response–recovery times increased with the operating temperature before it reached 120 °C, and after 120 °C, the response–recovery times decreased with the further increases in the operating temperature. Before the optimum operating temperature, the adsorption rate of the gas molecules was higher than the desorption rate, and the number of adsorbed oxygen ions and H₂S gas molecules on the material's surface increased, which led to the increase in the reaction time. With the increase in the operating temperature, the adsorption and desorption rates maintained a balance at the optimum operating temperature, and the number of H₂S gas molecules and adsorbed oxygen ions on the material's surface reached the maximum. At this operating temperature, the reaction time also reached the maximum. With the further increase in the operating temperature, the desorption rate of the gas molecules was higher than the adsorption rate, the reaction reactants became fewer and the reaction time became shorter. In addition, the response–recovery times of the 3 wt% Pd-LaFeO₃ were reduced by two times that of the pure LaFeO₃.

Table 3. The response and recovery times of Pd-LaFeO₃ to 1 ppm H₂S at different operating temperatures.

Time (s)	T (°C)						
	60	80	100	120	140	160	Pd (wt%)
Response	22.5	28.15	31.88	34.61	32.86	29.68	0
Recovery	18.26	22.31	25.88	26.63	25.5	23.37	0
Response	20.58	23.7	26.93	28.52	27.61	25.58	1
Recovery	18.01	20.56	21.83	22.97	21.86	19.51	1
Response	13.87	17.13	18.95	19.62	17.89	16.39	3
Recovery	10.68	12.75	14.26	15.22	14.5	13.16	3
Response	21.55	24.13	25.83	26.66	25.37	23.36	5
Recovery	15.65	16.92	18.16	18.83	17.76	15.33	5

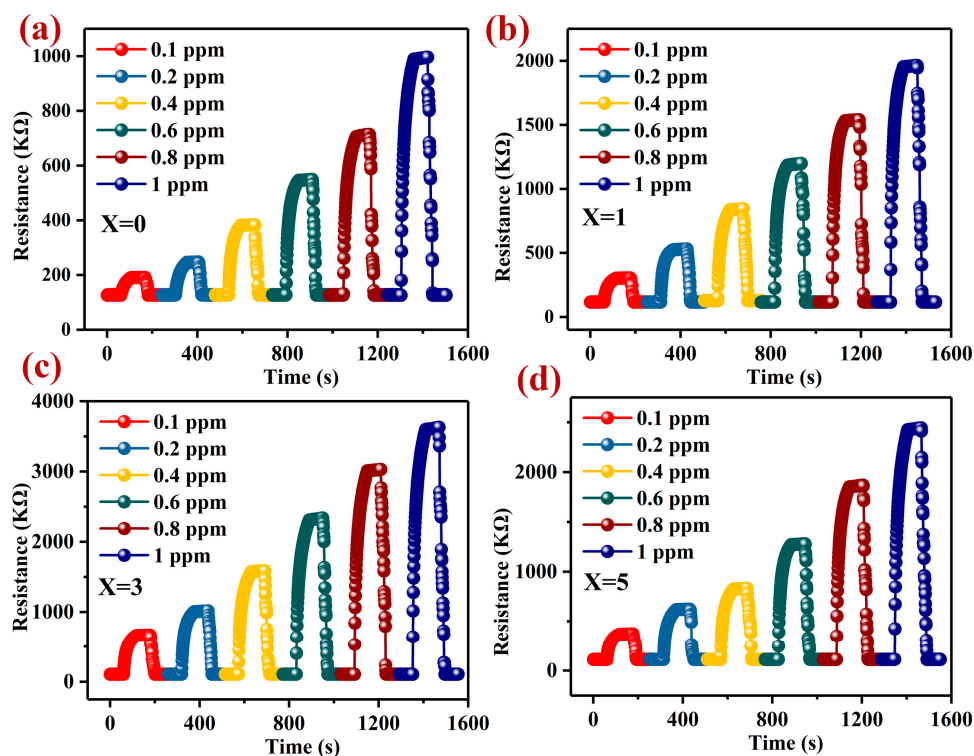


Figure 5. The dynamic resistances of LaFeO₃ with different amounts of Pd to different concentrations (0.1–1 ppm) of H₂S; X refers to the amount of Pd (a–d).

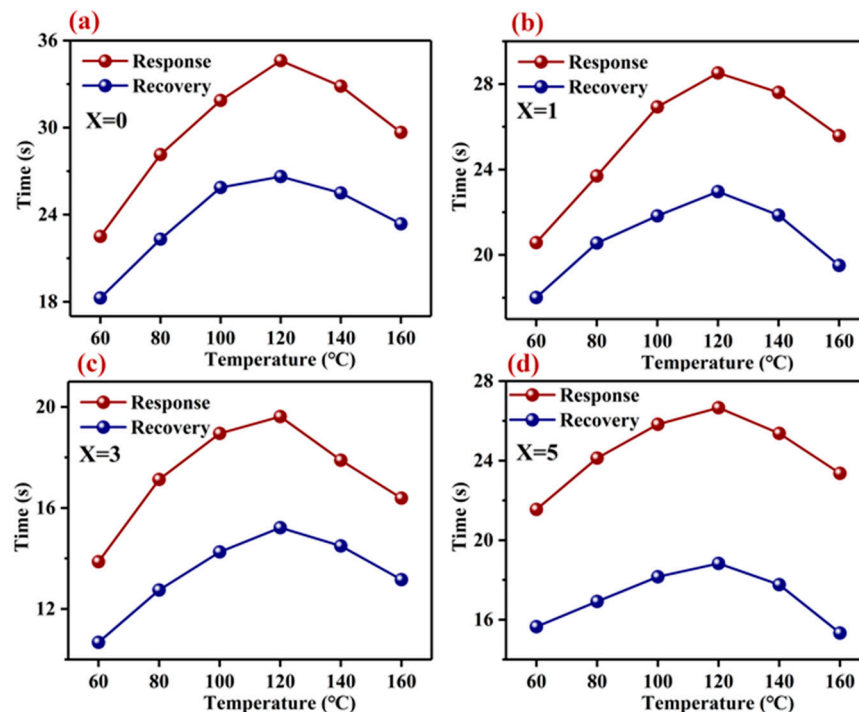


Figure 6. The response and recovery times of Pd–LaFeO₃ to 1 ppm H₂S at different operating temperatures; X refers to the amount of Pd (a–d).

In practical application, certain gases are commonly detected in mixtures, especially H₂S gas in a real person’s exhaled breath. Therefore, the selectivity of a gas-sensing material to a certain gas determines its practical application value. We present a selectivity comparison between 0–5 wt% Pd–LaFeO₃ to 1 ppm H₂S and several other common gases

in a person's exhaled breath in Figure 7a,d. Compared with other gases, Pd-LaFeO₃ has a high selectivity for H₂S gas. For N₂, O₂, NO, CO₂, CO and other common gases in a person's exhaled breath, the responses can be negligible, and the H₂S in the exhaled breath can more accurately be detected.

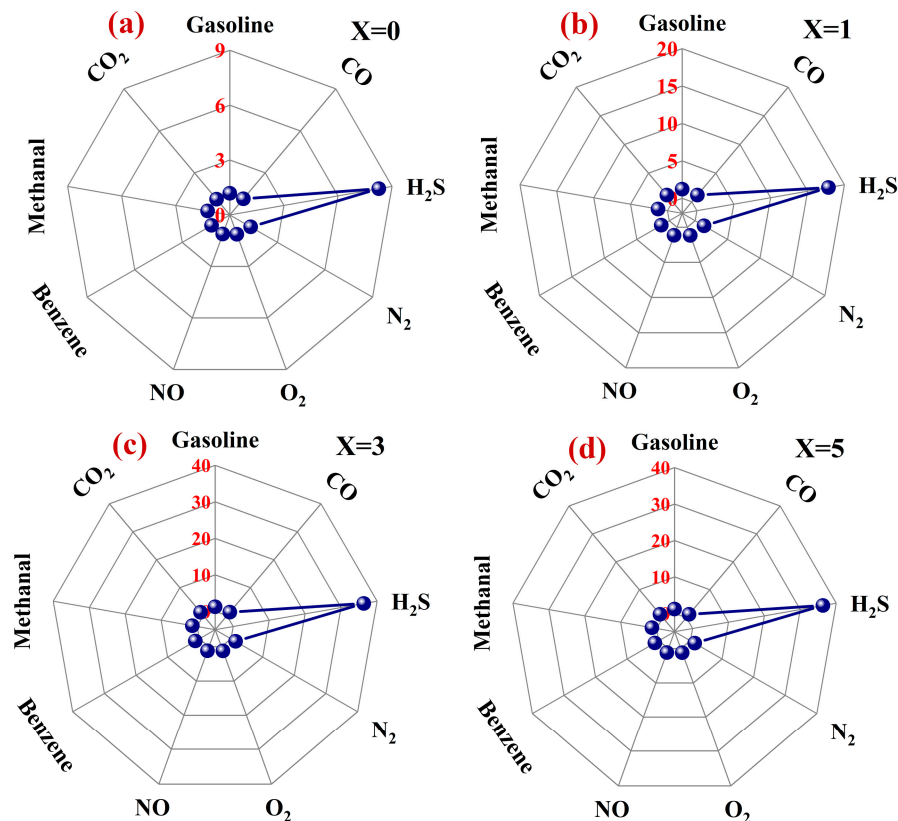
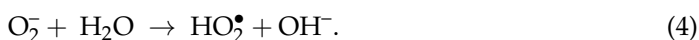


Figure 7. Selectivity comparison of 0–5 wt% Pd–LaFeO₃ to 1 ppm H₂S and several other common gases in a person's exhaled breath; X refers to the amount of Pd (a–d).

The relative humidity (RH) in the environment is also a factor that cannot be ignored in the application of gas sensors. In Figure 8a, we show the resistance changes of Pd–LaFeO₃ with the RH at 120 °C. For Pd–LaFeO₃, the resistance decreased with the RH, but the proportions of these decreases were different. In the 20–90% RH range, the proportions of the decreases were: 44.13% (0 wt% Pd), 34.1% (1 wt% Pd), 19.46% (3 wt% Pd) and 26.46% (5 wt% Pd), which means that the resistance of 3 wt% Pd–LaFeO₃ had the greatest RH adaptability. The RH can also affect the response of the gas-sensing material to the target gas. It has been demonstrated that oxygen (O₂) can capture the electrons from the surface of the materials to generate adsorbed oxygen (O₂[−]) which can further react with the surface-adsorbed water molecules (H₂O) to produce hydroxyl groups (OH[−]). Their reactions can be expressed as follows [53–57]:



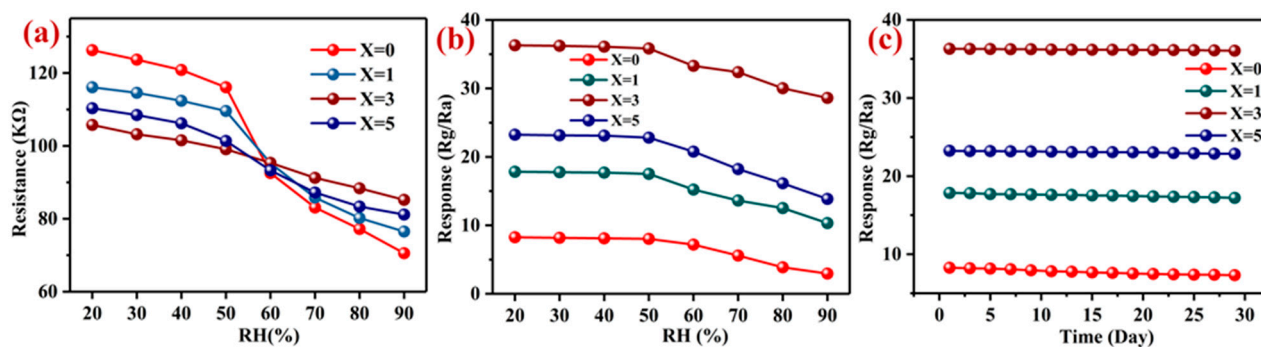


Figure 8. (a) Resistance curves of Pd–LaFeO₃ with RH; (b) response curves of Pd–LaFeO₃ with RH; (c) response curves of Pd–LaFeO₃ over time; X refers to the amount of Pd.

Based on the hydrogen bonding effect [53,57], the greater the number of hydroxyl groups, the more surface-absorbed water molecules and adsorbed oxygen there are, and the more holes are generated accordingly. Therefore, the resistance decreased with the RH.

In Figure 8b, we present the responses of Pd–LaFeO₃ to 1 ppm H₂S with RH. The responses decreased with the RH. Moreover, before 50% RH, the RH did not have a significant effect on the responses. However, after 50% RH, the responses decreased sharply, which means that the gas sensor used in this study can be used in low-RH environments without considering the influence of the RH. This feature greatly expands its practical applications in the field.

Long-term stability is another important property of gas-sensing materials. The higher the long-term stability, the longer the replacement cycle of the gas-sensing material, and the more economical and energy advantages it has. In Figure 8c, we show the long-term stability of Pd–LaFeO₃ over 30 days (pH = 6.8–7.3). The experimental data were recorded every two days. All the responses decreased slightly with time, but the proportions of the decreases were different, as follows: 11.45% (0 wt% Pd), 3.6% (1 wt% Pd), 0.65% (3 wt% Pd) and 1.63% (5 wt% Pd). The long-term stability of the 3 wt% Pd–LaFeO₃ was more than 17 times that of the pure LaFeO₃. LaFeO₃ with Pd presented greater advantages in terms of long-term stability.

4. Sensing-Mechanism Analysis

In Figure 9, we show the reaction mechanism of the whole experiment in this work. For a *p*-type semiconductor, the main carrier of Pd–LaFeO₃ is the hole (h^{\bullet}) (Figure 9a). The oxygen molecules that were adsorbed onto the surface of the Pd–LaFeO₃ continuously captured the electrons from the material, which caused an increase in the number of holes (Figure 9b). The rate at which the oxygen molecules captured electrons was slow at room temperature and had little effect on the resistance value. However, as the operating temperature gradually increased, the capture rating on the surface of Pd–LaFeO₃ increased. Therefore, the resistance decreased with the operating temperature (Figure 9c). In addition, the work function of the Pd was greater than the LaFeO₃, the free electron on the surface of the LaFeO₃ was much easier to transfer to the Pd nanoparticles and forming a depletion layer increased the material's resistance when it was in the air.

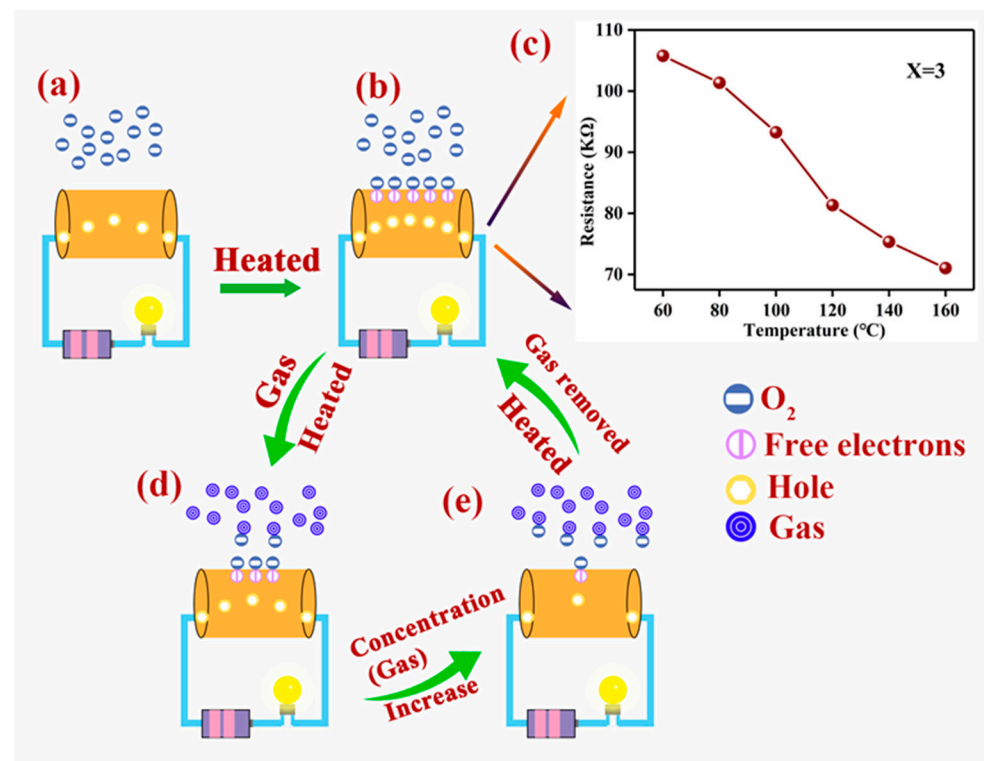
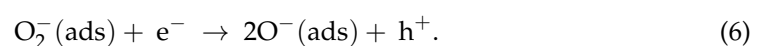
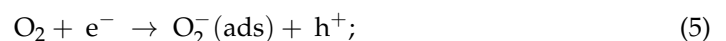


Figure 9. Reaction mechanism of the whole experiment in this work: (a) charge state on the surface of the material at room temperature; (b) charge state on the surface of the material under high temperature; (c) resistance curve of 3 wt% Pd–LaFeO₃ with operating temperatures; (d) change in charge state on surface of material after gas injection under high temperature; (e) change in charge state on surface of material with gas concentration under high temperature.

The reaction between the oxygen molecules and free electrons on the surface of the Pd–LaFeO₃ is as follows [58–60]:

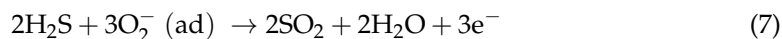


The ads refer to the state of the adsorbed oxygen on the surface of the LaFeO₃.

When the H₂S gas molecule was introduced, it was adsorbed onto the surface of the LaFeO₃ and reacted with the oxygen ions (Figure 9d). The adsorption and desorption on the surface of the Pd–LaFeO₃-to-H₂S gas molecules occurred simultaneously. The rates of adsorption and desorption increased with the operating temperature, and the rate of adsorption was greater than the rate of desorption before the operating temperature reached the optimum temperature. Therefore, the number of adsorbed H₂S molecules on the surface of the material increased, and the reaction between the H₂S molecules and oxygen ions was more intense, which resulted in response to the increase. When the operating temperature exceeded the optimum temperature, the rate of the adsorption of the Pd–LaFeO₃-to-H₂S molecules was lower than the rate of desorption, and the intensity of the reaction between the H₂S molecules and oxygen ions was reduced, which caused the response to decrease. Moreover, at the optimum temperature, as the concentration of H₂S gas molecules increased, this increased the number of adsorbed H₂S molecules on the surface of the Pd–LaFeO₃ and caused the response to increase (Figure 9e). However, the number of free electrons on the surface of the Pd–LaFeO₃ is not infinite, and the energy required to make an electronic transition within Pd–LaFeO₃ also increases. Therefore, the response (R_g/R_a) increased with the concentration of H₂S gas molecules, but the rate of increase declined. In addition, when the free electron was released from the adsorbed

oxygen ions to the Pd–LaFeO₃, the width of the LaFeO₃ in the depletion layer narrowed, which was caused by Pd, which resulted in a greater resistance change.

The reaction between the H₂S molecules and oxygen ions is as follows [30,31]:



5. Application in the Detection of H₂S

The accurate and quick assessment of the decomposition of meat and seafood is important. H₂S is among the most important gases released in the decomposition of food [30]. In this study, we detected the H₂S concentrations around shrimp over time using a gas sensor (Figure 10a) and GC–MS (GCMS-QP2020 NX), and we present the results in Figure 10b. There were nine shrimps in the experimental apparatus, each about 10–16 cm in length. We placed them on a plate in a closed test system (about 28 L). Point A refers to where the shrimp were placed. The concentration of H₂S increased with the time from death, and the concentration of H₂S measured by the gas sensor was greater than that measured by GC–MS at any time, which indicates that there were other gases in the air surrounding the shrimp that could have affected the gas sensor, but the effect was very small. We compared the H₂S concentrations measured by the two methods, and the error was within 10%. We present the results in Table 4.

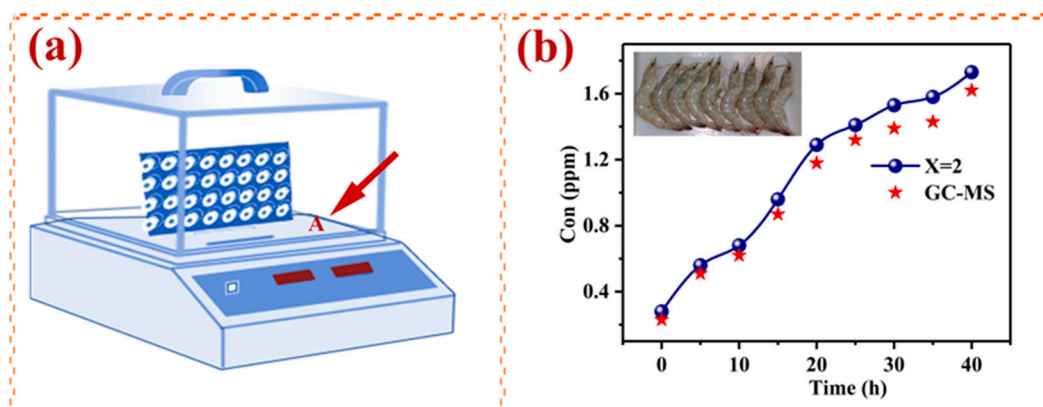


Figure 10. (a) Experimental setup used for H₂S detection of the emission of shrimps; (b) dynamic curve of H₂S concentration around shrimp with time.

Table 4. Concentration of H₂S obtained by gas sensor and GC–MS.

Method \ Time (h)	0	5	10	15	20	25	30	35	40
Gas sensor	0.28	0.56	0.68	0.96	1.29	1.41	1.53	1.58	1.73
GC–MS	0.23	0.51	0.62	0.87	1.18	1.32	1.39	1.43	1.62

6. Conclusions

In this study, we synthesized Pd modified LaFeO₃ with a large specific surface area and high porosity by the sol–gel method, which improved the response to a certain extent. According to the experimental results, the optimum Pd content is 3 wt%. The response of the 3 wt% Pd–LaFeO₃ to H₂S was more than four times higher than before modification with Pd, and the long-term stability was more than 17 times that of the pure LaFeO₃. Moreover, the response–recovery times of the 3 wt% Pd–LaFeO₃ were reduced by two times those of the pure LaFeO₃. In addition, the use of Pd modification as a catalyst greatly improved the RH adaptability and selectivity of the material. Finally, the Pd–LaFeO₃ was accurate in detecting the concentration of H₂S gas in the air around the shrimp, with

an error of less than 10%, compared with the results obtained by GC–MS. According to the experimental results, noble metal surface modification improves the performance of gas-sensing materials, and Pd–LaFeO₃ has great potential for H₂S detection.

Author Contributions: Writing—original draft, H.Z. and J.X.; conceptualization, H.Z., D.S., S.L. and J.C.; resource and data curation, H.Z., T.H., Y.W., L.Z. and S.Y.; writing—correction and editing, H.Z., J.C., D.S. and J.X. All authors have read and agreed to the published version of the manuscript.

Funding: This work was supported by the Shandong Natural Science Foundation (No. ZR2021QE265), the Fundamental Research Funds of Taishan University (No. Y-01-2020015), the National Natural Science Foundation of China (Nos. 61574098 and 61204051), the Shandong Province Key Research and Development Program (No. 2019GGX101016) and the National Natural Science Foundation of China (51901160).

Institutional Review Board Statement: Not applicable.

Informed Consent Statement: Not applicable.

Data Availability Statement: Not applicable.

Conflicts of Interest: The authors declare no conflict of interest.

References

1. Zuo, P.; Wang, R.; Li, F.; Wu, F.; Xu, G.; Niu, W. A Trace Ppb-Level Electrochemical H₂S Sensor Based on Ultrathin Pt Nanotubes. *Talanta* **2021**, *233*, 122539. [[CrossRef](#)] [[PubMed](#)]
2. Kumar, V.; Majhi, S.M.; Kim, K.-H.; Kim, H.W.; Kwon, E.E. Advances in In₂O₃-Based Materials for the Development of Hydrogen Sulfide Sensors. *Chem. Eng. J.* **2021**, *404*, 126472. [[CrossRef](#)]
3. Li, X.; Hu, J.; Ban, J.; He, S.; Zheng, N.; Shao, G.; Cao, G. Mechanism of Enhanced H₂S Sensor Ability Based on Emerging Li_{0.5}La_{0.5}TiO₃-SnO₂ Core-Shell Structure. *Sens. Actuators B Chem.* **2022**, *352*, 131054. [[CrossRef](#)]
4. Priya, A.K.; Suresh, R.; Kumar, P.S.; Rajendran, S.; Vo, D.-V.N.; Soto-Moscoso, M. A Review on Recent Advancements in Photocatalytic Remediation for Harmful Inorganic and Organic Gases. *Chemosphere* **2021**, *284*, 131344. [[CrossRef](#)] [[PubMed](#)]
5. Liu, B.; Zhang, L.; Luo, Y.; Gao, L.; Duan, G. The Dehydrogenation of H-S Bond into Sulfur Species on Supported Pd Single Atoms Allows Highly Selective and Sensitive Hydrogen Sulfide Detection. *Small* **2021**, *17*, 2105643. [[CrossRef](#)]
6. Zheng, X.; Zhang, G.; Yao, Z.; Zheng, Y.; Shen, L.; Liu, F.; Cao, Y.; Liang, S.; Xiao, Y.; Jiang, L. Engineering of Crystal Phase over Porous MnO₂ with 3D Morphology for Highly Efficient Elimination of H₂S. *J. Hazard. Mater.* **2021**, *411*, 125180. [[CrossRef](#)]
7. Ethiraj, J.; Bonino, F.; Lamberti, C.; Bordiga, S. H₂S Interaction with HKUST-1 and ZIF-8 MOFs: A Multitechnique Study. *Microporous Mesoporous Mater.* **2015**, *207*, 90–94. [[CrossRef](#)]
8. Wu, X.; Xiong, S.; Gong, Y.; Gong, Y.; Wu, W.; Mao, Z.; Liu, Q.; Hu, S.; Long, X. MOF-SMO Hybrids as a H₂S Sensor with Superior Sensitivity and Selectivity. *Sens. Actuators B Chem.* **2019**, *292*, 32–39. [[CrossRef](#)]
9. Chen, L.; Luque, R.; Li, Y. Controllable Design of Tunable Nanostructures inside Metal–Organic Frameworks. *Chem. Soc. Rev.* **2017**, *46*, 4614–4630. [[CrossRef](#)]
10. Lopez, J.D.; Keley, M.; Dante, A.; Werneck, M.M. Optical Fiber Sensor Coated with Copper and Iron Oxide Nanoparticles for Hydrogen Sulfide Sensing. *Opt. Fiber Technol.* **2021**, *67*, 102731. [[CrossRef](#)]
11. Hsu, K.-C.; Fang, T.-H.; Hsiao, Y.-J.; Li, Z.-J. Rapid Detection of Low Concentrations of H₂S Using CuO-Doped ZnO Nanofibers. *J. Alloys Compd.* **2021**, *852*, 157014. [[CrossRef](#)]
12. Yaegaki, K.; Sanada, K. Volatile Sulfur Compounds in Mouth Air from Clinically Healthy Subjects and Patients with Periodontal Disease. *J. Periodontal Res.* **1992**, *27*, 233–238. [[CrossRef](#)] [[PubMed](#)]
13. Jaouali, I.; Hamrouni, H.; Moussa, N.; Nsib, M.F.; Centeno, M.A.; Bonavita, A.; Neri, G.; Leonardi, S.G. LaFeO₃ Ceramics as Selective Oxygen Sensors at Mild Temperature. *Ceram. Int.* **2018**, *44*, 4183–4189. [[CrossRef](#)]
14. Ma, Z.; Yang, K.; Xiao, C.; Jia, L. C-Doped LaFeO₃ Porous Nanostructures for Highly Selective Detection of Formaldehyde. *Sens. Actuators B Chem.* **2021**, *347*, 130550. [[CrossRef](#)]
15. Xiangfeng, C.; Siciliano, P. CH₃SH-Sensing Characteristics of LaFeO₃ Thick-Film Prepared by Co-Precipitation Method. *Sens. Actuators B Chem.* **2003**, *94*, 197–200. [[CrossRef](#)]
16. Song, P.; Zhang, H.; Han, D.; Li, J.; Yang, Z.; Wang, Q. Preparation of Biomorphic Porous LaFeO₃ by Sorghum Straw Biotemplate Method and Its Acetone Sensing Properties. *Sens. Actuators B Chem.* **2014**, *196*, 140–146. [[CrossRef](#)]
17. Hosoya, Y.; Itagaki, Y.; Aono, H.; Sadaoka, Y. Ozone Detection in Air Using SmFeO₃ Gas Sensor. *Sens. Actuators B Chem.* **2005**, *108*, 198–201. [[CrossRef](#)]
18. Huang, H.T.; Zhang, W.L.; Zhang, X.D.; Guo, X. NO₂ Sensing Properties of SmFeO₃ Porous Hollow Microspheres. *Sens. Actuators B Chem.* **2018**, *265*, 443–451. [[CrossRef](#)]
19. Tomoda, M.; Okano, S.; Itagaki, Y.; Aono, H.; Sadaoka, Y. Air Quality Prediction by Using Semiconducting Gas Sensor with Newly Fabricated SmFeO₃ Film. *Sens. Actuators B Chem.* **2004**, *97*, 190–197. [[CrossRef](#)]

20. Han, T.; Ma, S.Y.; Xu, X.L.; Xu, X.H.; Pei, S.T.; Tie, Y.; Cao, P.F.; Liu, W.W.; Wang, B.J.; Zhang, R.; et al. Rough SmFeO₃ Nanofibers as an Optimization Ethylene Glycol Gas Sensor Prepared by Electrospinning. *Mater. Lett.* **2020**, *268*, 127575. [[CrossRef](#)]
21. Gaiardo, A.; Zonta, G.; Gherardi, S.; Malagù, C.; Fabbri, B.; Valt, M.; Vanzetti, L.; Landini, N.; Casotti, D.; Cruciani, G.; et al. Nanostructured SmFeO₃ Gas Sensors: Investigation of the Gas Sensing Performance Reproducibility for Colorectal Cancer Screening. *Sensors* **2020**, *20*, 5910. [[CrossRef](#)] [[PubMed](#)]
22. Ma, L.; Ma, S.Y.; Shen, X.F.; Wang, T.T.; Jiang, X.H.; Chen, Q.; Qiang, Z.; Yang, H.M.; Chen, H. PrFeO₃ Hollow Nanofibers as a Highly Efficient Gas Sensor for Acetone Detection. *Sens. Actuators B Chem.* **2018**, *255*, 2546–2554. [[CrossRef](#)]
23. Pei, S.; Ma, S.; Xu, X.; Xu, X.; Almamoun, O. Modulated PrFeO₃ by Doping Sm³⁺ for Enhanced Acetone Sensing Properties. *J. Alloys Compd.* **2021**, *856*, 158274. [[CrossRef](#)]
24. Song, Y.; Zhang, Y.; Ma, M.; Ren, J.; Liu, C.; Tan, J. Visible Light-Assisted Formaldehyde Sensor Based on HoFeO₃ Nanoparticles with Sub-Ppm Detection Limit. *Ceram. Int.* **2020**, *46*, 16337–16344. [[CrossRef](#)]
25. Sheng, H.; Ma, S.; Han, T.; Yun, P.; Yang, T.; Ren, J. A Highly Sensitivity and Anti-Humidity Gas Sensor for Ethanol Detection with NdFeO₃ Nano-Coral Granules. *Vacuum* **2022**, *195*, 110642. [[CrossRef](#)]
26. Addabbo, T.; Bertocci, F.; Fort, A.; Gregorkiewitz, M.; Mugnaini, M.; Spinicci, R.; Vignoli, V. Gas Sensing Properties and Modeling of YCoO₃ Based Perovskite Materials. *Sens. Actuators B Chem.* **2015**, *221*, 1137–1155. [[CrossRef](#)]
27. Cerdà, J.; Arbiol, J.; Dezanneau, G.; Diaz, R.; Morante, J.R. Perovskite-Type BaSnO₃ Powders for High Temperature Gas Sensor Applications. *Sens. Actuators B Chem.* **2002**, *84*, 21–25. [[CrossRef](#)]
28. Yin, Y.; Shen, Y.; Zhou, P.; Lu, R.; Li, A.; Zhao, S.; Liu, W.; Wei, D.; Wei, K. Fabrication, Characterization and n-Propanol Sensing Properties of Perovskite-Type ZnSnO₃ Nanospheres Based Gas Sensor. *Appl. Surf. Sci.* **2020**, *509*, 145335. [[CrossRef](#)]
29. Balamurugan, C.; Lee, D.-W. Perovskite Hexagonal YMnO₃ Nanopowder as P-Type Semiconductor Gas Sensor for H₂S Detection. *Sens. Actuators B Chem.* **2015**, *221*, 857–866. [[CrossRef](#)]
30. Zhou, Q.; Xu, L.; Kan, Z.; Yang, L.; Chang, Z.; Dong, B.; Bai, X.; Lu, G.; Song, H. A Multi-Platform Sensor for Selective and Sensitive H₂S Monitoring: Three-Dimensional Macroporous ZnO Encapsulated by MOFs with Small Pt Nanoparticles. *J. Hazard. Mater.* **2022**, *426*, 128075. [[CrossRef](#)]
31. Bae, G.; Kim, M.; Lee, A.; Ji, S.; Jang, M.; Yim, S.; Song, W.; Lee, S.S.; Yoon, D.H.; An, K.S. Nanometric Lamination of Zinc Oxide Nanofilms with Gold Nanoparticles for Self-Perceived Periodontal Disease Sensors. *Compos. Part B Eng.* **2022**, *230*, 109490. [[CrossRef](#)]
32. Fan, J.; Liu, P.; Chen, X.; Zhou, H.; Fu, S.; Wu, W. Carbon Nanotubes-CuO/SnO₂ Based Gas Sensor for Detecting H₂S in Low Concentration. *Nanotechnology* **2019**, *30*, 475501. [[CrossRef](#)] [[PubMed](#)]
33. Yao, X.; Zhao, J.; Liu, J.; Wang, F.; Wu, L.; Meng, F.; Zhang, D.; Wang, R.; Ahmed, J.; Ojha, K. H₂S Sensing Material Pt-WO₃ Nanorods with Excellent Comprehensive Performance. *J. Alloys Compd.* **2022**, *900*, 163398. [[CrossRef](#)]
34. Akamatsu, T.; Itoh, T.; Tsuruta, A.; Masuda, Y. CH₃SH and H₂S Sensing Properties of V₂O₅/WO₃/TiO₂ Gas Sensor. *Chemosensors* **2021**, *9*, 113. [[CrossRef](#)]
35. Li, X.; Yang, H.; Wang, X.; Qin, Z.; Hu, X.; Wang, X.; Xie, C.; Zeng, D. Exposed Edges of Porous Ultrathin WO₃ Nanosheets Determined High-Performance Sensing for Hydrogen Sulfide. *Appl. Surf. Sci.* **2022**, *571*, 151327. [[CrossRef](#)]
36. Wang, Q.; Huang, J.; Zhou, J.; Liu, Z.; Geng, Y.; Liang, Z.; Du, Y.; Tian, X. Different Nanostructured Tungsten Oxides Synthesized by Facile Solvothermal Route for Chlorine Gas Sensing. *Sens. Actuators B Chem.* **2018**, *275*, 306–311. [[CrossRef](#)]
37. Guo, L.; Xie, N.; Wang, C.; Kou, X.; Ding, M.; Zhang, H.; Sun, Y.; Song, H.; Wang, Y.; Lu, G. Enhanced Hydrogen Sulfide Sensing Properties of Pt-Functionalized α-Fe₂O₃ Nanowires Prepared by One-Step Electrospinning. *Sens. Actuators B Chem.* **2018**, *255*, 1015–1023. [[CrossRef](#)]
38. Lim, K.; Jo, Y.M.; Kim, S.; Yoon, J.W.; Jeong, S.Y.; Kim, J.S.; Choi, H.J.; Cho, Y.; Park, J.; Jeong, Y.W.; et al. Selective Dual Detection of Hydrogen Sulfide and Methyl Mercaptan Using CuO/CuFe₂O₄ Nanopattern Chemiresistors. *Sens. Actuators B Chem.* **2021**, *348*, 130665. [[CrossRef](#)]
39. Senapati, M.; Sahu, P.P. Meat Quality Assessment Using Au Patch Electrode Ag-SnO₂/SiO₂/Si MIS Capacitive Gas Sensor at Room Temperature. *Food Chem.* **2020**, *324*, 126893. [[CrossRef](#)]
40. Gao, H.; Wei, D.; Lin, P.; Liu, C.; Sun, P.; Shimano, K.; Yamazoe, N.; Lu, G. The Design of Excellent Xylene Gas Sensor Using Sn-Doped NiO Hierarchical Nanostructure. *Sens. Actuators B Chem.* **2017**, *253*, 1152–1162. [[CrossRef](#)]
41. Guo, L.; Shen, Z.; Ma, C.; Ma, C.; Wang, J.; Yuan, T. Gas Sensor Based on MOFs-Derived Au-Loaded SnO₂ Nanosheets for Enhanced Acetone Detection. *J. Alloys Compd.* **2022**, *906*, 164375. [[CrossRef](#)]
42. Fan, X.; Xu, Y.; Ma, C.; He, W. In-Situ Growth of Co₃O₄ Nanoparticles Based on Electrospray for an Acetone Gas Sensor. *J. Alloys Compd.* **2021**, *854*, 157234. [[CrossRef](#)]
43. Chen, L.; Song, Y.; Liu, W.; Dong, H.; Wang, D.; Liu, J.; Liu, Q.; Chen, X. MOF-Based Nanoscale Pt Catalyst Decorated SnO₂ Porous Nanofibers for Acetone Gas Detection. *J. Alloys Compd.* **2022**, *893*, 162322. [[CrossRef](#)]
44. Zhu, H.; Haidry, A.A.; Wang, Z.; Ji, Y. Improved Acetone Sensing Characteristics of TiO₂ Nanobelts with Ag Modification. *J. Alloys Compd.* **2021**, *887*, 161312. [[CrossRef](#)]
45. Liu, G.; Zhu, L.; Yu, Y.; Qiu, M.; Gao, H.; Chen, D. WO₃ Nanoplates for Sensitive and Selective Detections of Both Acetone and NH₃ Gases at Different Operating Temperatures. *J. Alloys Compd.* **2021**, *858*, 157638. [[CrossRef](#)]
46. Yang, M.; Zhang, S.; Qu, F.; Gong, S.; Wang, C.; Qiu, L.; Yang, M.; Cheng, W. High Performance Acetone Sensor Based on ZnO Nanorods Modified by Au Nanoparticles. *J. Alloys Compd.* **2019**, *797*, 246–252. [[CrossRef](#)]

47. Zhu, Z.; Li, Z.; Xiong, X.; Hu, X.; Wang, X.; Li, N.; Jin, T.; Chen, Y. ZnO/ZnSe Heterojunction Nanocomposites with Oxygen Vacancies for Acetone Sensing. *J. Alloys Compd.* **2022**, *906*, 164316. [[CrossRef](#)]
48. Yuan, Z.; Feng, Z.; Kong, L.; Zhan, J.; Ma, X. Simple Synthesis of Porous ZnO Nanoplates Hyper-Doped with Low Concentration of Pt for Efficient Acetone Sensing. *J. Alloys Compd.* **2021**, *865*, 158890. [[CrossRef](#)]
49. Zhang, H.J.; Liu, L.Z.; Zhang, X.R.; Zhang, S.; Meng, F.N. Microwave-Assisted Solvothermal Synthesis of Shape-Controlled CoFe₂O₄ Nanoparticles for Acetone Sensor. *J. Alloys Compd.* **2019**, *788*, 1103–1112. [[CrossRef](#)]
50. Hanh, N.H.; Van Duy, L.; Hung, C.M.; Xuan, C.T.; Van Duy, N.; Hoa, N.D. High-Performance Acetone Gas Sensor Based on Pt-Zn₂SnO₄ Hollow Octahedra for Diabetic Diagnosis. *J. Alloys Compd.* **2021**, *886*, 161284. [[CrossRef](#)]
51. Wang, X.; Qin, H.; Pei, J.; Chen, Y.; Li, L.; Xie, J.; Hu, J. Sensing Performances to Low Concentration Acetone for Palladium Doped LaFeO₃ Sensors. *J. Rare Earths* **2016**, *34*, 704–710. [[CrossRef](#)]
52. Ghasdi, M.; Alamdari, H. Highly Sensitive Pure and Pd-Doped LaFeO₃ Nanocrystalline Perovskitebased Sensor Prepared by High Energy Ball Milling. *Adv. Mater. Res.* **2012**, *409*, 486–491. [[CrossRef](#)]
53. Zhang, Y.; Zou, H.; Peng, J.; Duan, Z.; Ma, M.; Xin, X.; Li, W.; Zheng, X. Enhanced Humidity Sensing Properties of SmFeO₃-Modified MoS₂ Nanocomposites Based on the Synergistic Effect. *Sens. Actuators B Chem.* **2018**, *272*, 459–467. [[CrossRef](#)]
54. Zhang, P.; Qin, H.; Lv, W.; Zhang, H.; Hu, J. Gas Sensors Based on Ytterbium Ferrites Nanocrystalline Powders for Detecting Acetone with Low Concentrations. *Sens. Actuators B Chem.* **2017**, *246*, 9–19. [[CrossRef](#)]
55. Wang, J.; Wu, F.Q.; Shi, K.H.; Wang, X.H.; Sun, P.P. Humidity Sensitivity of Composite Material of Lanthanum Ferrite/Polymer Quaternary Acrylic Resin. *Sens. Actuators B Chem.* **2004**, *99*, 586–591. [[CrossRef](#)]
56. Zhao, J.; Liu, Y.; Li, X.; Lu, G.; You, L.; Liang, X.; Liu, F.; Zhang, T.; Du, Y. Highly Sensitive Humidity Sensor Based on High Surface Area Mesoporous LaFeO₃ Prepared by a Nanocasting Route. *Sens. Actuators B Chem.* **2013**, *181*, 802–809. [[CrossRef](#)]
57. Fan, S.X.; Tang, W. Synthesis, Characterization and Mechanism of Electrospun Carbon Nanofibers Decorated with ZnO Nanoparticles for Flexible Ammonia Gas Sensors at Room Temperature. *Sens. Actuators B Chem.* **2022**, *362*, 131789. [[CrossRef](#)]
58. Zhang, L.; Qin, H.; Song, P.; Hu, J.; Jiang, M. Electric Properties and Acetone-Sensing Characteristics of La_{1-x}Pb_xFeO₃ Perovskite System. *Mater. Chem. Phys.* **2006**, *98*, 358–362. [[CrossRef](#)]
59. Liu, X.; Hu, J.; Cheng, B.; Qin, H.; Jiang, M. Acetone Gas Sensing Properties of SmFe_{1-x}Mg_xO₃ Perovskite Oxides. *Sens. Actuators B Chem.* **2008**, *134*, 483–487. [[CrossRef](#)]
60. Wang, X.; Ma, W.; Sun, K.; Hu, J.; Qin, H. Nanocrystalline Gd_{1-x}Ca_xFeO₃ Sensors for Detection of Methanol Gas. *J. Rare Earths* **2017**, *35*, 690–696. [[CrossRef](#)]